pubs.acs.org/JPCC

Article

# Exploring the Photocatalytic Potential of Lead-Free Cs<sub>2</sub>Ag<sub>x</sub>Na<sub>1-x</sub>BiCl<sub>6</sub> Double Perovskites: Influence of Ag/Na Composition and Nanocrystalline Heterojunction Formation Induced by In Situ Water Interaction

Luan do Nascimento Passini, Bianca Oliveira Mattos, Jéssica de Bona, Luis Henrique da Silveira Lacerda, Ubirajara Pereira Rodrigues-Filho, Elias Paiva Ferreira-Neto,\* and Danilo Manzani\*



Downloaded via UNIV OF SAO PAULO on September 30, 2025 at 12:00:59 (UTC). See https://pubs.acs.org/sharingguidelines for options on how to legitimately share published articles.

Cite This: J. Phys. Chem. C 2025, 129, 16719-16732



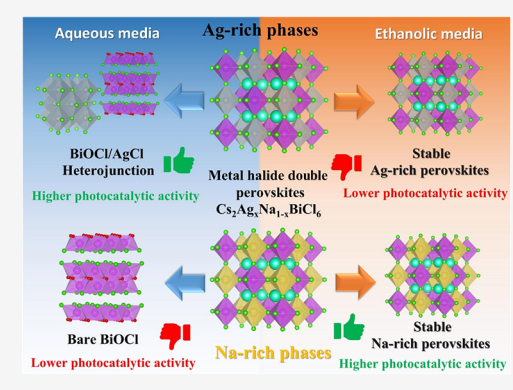
**ACCESS** I

Metrics & More

Article Recommendations

Supporting Information

ABSTRACT: Lead-free halide double perovskites (A2BIBIIIX6) have recently emerged as promising candidates in photocatalysis, demonstrating potential for applications such as CO<sub>2</sub> photoreduction, H<sub>2</sub> evolution, and organic pollutant degradation. However, the influence of monovalent metal cation composition, particularly Ag<sup>+</sup> and Na<sup>+</sup>, on their photoactivity performance remains poorly understood, and their behavior in aqueous media has been insufficiently explored. In this study, we synthesized double perovskites, Cs<sub>2</sub>Ag<sub>x</sub>Na<sub>1-x</sub>BiCl<sub>6</sub>, with varying Ag/Na ratios and systematically evaluated their photocatalytic activity in both aqueous and ethanolic environments. Density Functional Theory (DFT) simulations were conducted to analyze their electronic structures and charge carrier stability. By correlating experimental characterization, theoretical calculations, and photocatalytic performance, we uncovered critical insights into the role of Ag<sup>+</sup> and Na<sup>+</sup> in tuning the photoactivity of these lead-free perovskites.



Our results indicate that increasing the Ag+ content reduces the intrinsic photocatalytic activity of Bi-based double perovskites in ethanolic media, a trend attributed to changes in charge carrier stability, according to DFT. In contrast, the opposite effect was observed in aqueous media, where higher Ag<sup>+</sup> concentrations enhanced photocatalytic performance. This behavior was linked to the complete structural conversion of the perovskite in water, leading to the in situ formation of a BiOCl/AgCl heterojunction with superior photocatalytic properties. These findings offer valuable insights into the interplay between composition, water stability, and photocatalytic efficiency, providing a foundation for the rational design of advanced photocatalysts derived from lead-free metal halide double perovskites.

## 1. INTRODUCTION

The rapid growth of industrial development and population has led to an increased usage of heavy metals, pesticides, insecticides, and textile dyes, which are contaminants that pose significant environmental risks.<sup>1,2</sup> Conventional water treatment methods often struggle to completely remove these highly toxic anthropogenic organic pollutants, especially at low concentrations, highlighting the urgent need for more effective water decontamination strategies.3 Heterogeneous photocatalysis has emerged as a promising solution to this challenge, offering a cost-effective and sustainable approach by harnessing renewable solar energy to degrade organic pollutants. Its high efficiency and environmentally friendly nature make it an attractive alternative for water purification.<sup>4,5</sup> Ideally, promising photocatalysts exhibit remarkable solar energy absorption, high quantum efficiency, chemical stability, and nontoxicity. Heterogeneous photocatalytic reactions occur on the surface of a semiconductor when it is exposed to light with an energy equal to or greater than its bandgap. This process generates

photoexcited electron-hole pairs (e<sup>-</sup> and h<sup>+</sup>), which, in turn, react with adsorbed molecules to produce reactive species capable of degrading pollutants. Various semiconductor photocatalysts have been explored for organic pollutant degradation, including ZnO,<sup>7</sup> CdS,<sup>8</sup> MoS<sub>2</sub>,<sup>9</sup> WO<sub>3</sub>,<sup>10</sup> TiO<sub>2</sub>-based nanomaterials.<sup>11–13</sup> More recently, metal halide double perovskites have gained attention for their promising photocatalytic performance in various applications.

Metal halide perovskites (MHPs), particularly Pb-based perovskites, have garnered significant attention from the scientific community due to their exceptional optical and electronic properties. These materials exhibit high absorption

Received: May 3, 2025 Revised: September 1, 2025

Accepted: September 2, 2025

Published: September 9, 2025





efficiency in the ultraviolet-visible (UV-vis) range, low exciton binding energy, high charge carrier mobility, slow electron-hole recombination, bright photoluminescence, and a tunable bandgap. 14-16 These outstanding optoelectronic properties position metal halide perovskites (MHPs) as leading candidates for the next generation of high-performance solar cells and key materials in photonics for developing luminescent materials and optical devices. MHPs adopt the general formula ABX<sub>3</sub>, featuring a perovskite-type structure where the A-site is occupied by a monovalent cation, which can be organic, such as CH<sub>3</sub>NH<sub>3</sub><sup>+</sup> (MA) and CH(NH<sub>2</sub>)<sub>2</sub><sup>+</sup> (FA) or inorganic as Cs<sup>+</sup>. The B-site is typically occupied by a divalent cation  $(Pb^{2+})$ , while the X-site consists of halide anions  $(Cl^-, Br^-, or \ I^-)$ . Furthermore, MHPs have recently emerged as promising photocatalysts for various applications. In 2016, Park et al. first reported the photocatalytic activity of MHPs for HI photolysis, 18 marking the onset of research into their photocatalytic potential. Since then, numerous studies have demonstrated the use of MHPs in H<sub>2</sub> production, <sup>19</sup> CO<sub>2</sub> photoreduction,<sup>20</sup> and the degradation of organic pollutants.<sup>21</sup> However, a major drawback of MHPs is their inherent instability in humid environments and their poor water tolerance, leading to the leaching of water-soluble Pb<sup>2+</sup>, which poses serious environmental and health concerns. One effective strategy to address this issue is the heterovalent substitution of lead with two other metals, forming a double perovskite structure (A<sub>2</sub>B<sup>I</sup>B<sup>III</sup>X<sub>6</sub>).<sup>25</sup> In halide double perovskites, the A-site is commonly occupied by Cs<sup>+</sup>, MA or FA; the B<sup>I</sup>-site by a monovalent cation (Cu<sup>+</sup>, Ag<sup>+</sup> or Au<sup>+</sup>), and the B<sup>III</sup>site by a trivalent cation (Bi<sup>3+</sup>, Sb<sup>3+</sup> or In<sup>3+</sup>), while the X-site consists of halide anions (Cl-, Br- or I-). Among these, Bibased double perovskites stand out as particularly attractive candidates due to lower toxicity and to the similarities between Bi<sup>3+</sup> and Pb<sup>2+</sup>, including comparable ionic radius, similar electronic configuration, and electronegativity.<sup>26</sup>

Leveraging this strategy, Ag/Bi-based double metal halide perovskites, such as Cs<sub>2</sub>AgBiBr<sub>6</sub> and Cs<sub>2</sub>AgBiCl<sub>6</sub>, have been proposed as promising candidates to Pb-based metal halide perovskites (MHPs), exhibiting comparable optoelectronic properties along with enhanced stability. In 2023, Guo et al. reported Cs<sub>2</sub>AgBiCl<sub>6</sub> as a highly efficient photocatalyst for organic pollutant degradation. Furthermore, cation mixing plays a crucial role in tuning the semiconductor's bandgap energy. In 2021, Dakshinamurthy et al. demonstrated bandgap modulation from 2.64 to 3.01 eV by replacing  $Ag^+$  for  $Na^+$  in the  $Cs_2Ag_{1-x}Na_xBiCl_6$  lattice. However, despite these promising findings the photocatalytic properties of Bi-based perovskites remain largely unexplored. While Guo et al. reported materials stability, their photocatalytic experiments were conducted exclusively in ethanolic media, leaving the behavior in aqueous environments unexplored. Although this study represents an important step forward, evaluating these materials in aqueous media is crucial for practical applications in water purification through photocatalytic organic pollutant degradation. Additionally, the specific role of Ag/Na in the photocatalytic performance of double perovskites remains unclear, as other metal-ion-substituted Bi-based double perovskite structures have yet to be explored for photocatalytic applications.

Herein, we report the synthesis of  $Cs_2Ag_xNa_{1-x}BiCl_6$  via a wet chemical route to investigate the influence of Ag and Na content on the photocatalytic performance of Bibased double perovskites. Density Functional Theory (DFT) simulations

were employed to explore the electronic structures and charge carrier dynamics of these materials. Photocatalytic experiments were conducted in both  $\rm H_2O$  and EtOH media, revealing distinct trends in stability and photocatalytic efficiency. Notably, higher Ag content enhanced photocatalytic activity in aqueous media but reduced it in ethanol. These intriguing and contrasting behaviors are discussed in terms of the *in situ* formation of a BiOCl/AgCl heterojunction in water and insights from DFT analysis. Overall, this study provides a deeper understanding of the intricate relationships between composition, water stability, electronic structure, and photocatalytic behavior in Bi-based double perovskites, offering valuable guidelines for the rational design of next-generation photocatalysts.

# 2. EXPERIMENTAL SECTION

**2.1. Reagents.** HCl (Aldrich, 37%), CsCl (Vetec, P.A.), AgCl (Aldrich, 99%), BiCl<sub>3</sub> (Aldrich, ≥98%), NaCl (Synth, P.A.-A.C.S.), isopropyl alcohol (Exodo, 99.5%) were purchased and used as received.

2.2. Synthesis of the Bibased Double Halide Perovskites. Perovskite samples were synthesized via a modified aqueous solution method, adapted from Chini et al.<sup>2</sup> Cs<sub>2</sub>AgBiCl<sub>6</sub> was prepared by dissolving stoichiometric amounts of AgCl (172 mg, 10 mM) and BiCl<sub>3</sub> (378 mg, 10 mM) in a 1:1 molar ratio into 120 mL of an acidic solution consisting of 100 mL of HCl (37%) and 20 mL of Milli-Q water (18.2 M $\Omega$ · cm), under vigorous stirring at 348 K for 15 min. After complete dissolution, 404.1 mg of CsCl (20 mM) was added to the solution, followed by heating at 383 K for 1 h, and then cooled to room temperature. The resulting yellowish solid was collected, washed with isopropyl alcohol, centrifuged, and dried at 383 K overnight. For mixed compositions, Ag and Na concentrations were stoichiometrically adjusted (addition of AgCl or NaCl) to obtain  $Cs_2Ag_xNa_{1-x}BiCl_6$  with x = 1.0; 0.8; 0.6; 0.5; 0.4; 0.2; and 0.0, labeled as Ag1.0, Ag0.8, Ag0.6, Ag0.5, Ag0.4, Ag0.2, and Ag0.0, respectively.

**2.3. Materials Characterization.** Powder X-ray diffraction (XRD) analysis of the polycrystalline Bi-based perovskite samples was carried out using a Bruker D8 Advance diffractometer equipped with a Cu-K $\alpha$  monochromator ( $\lambda$  = 1.5418 Å). Measurements were conducted at room temperature over the  $2\theta$  range of 10 to 60°, with a scan step width of 0.02° and an angular rate of 0.5 s step<sup>-1</sup>, using a LynxEye position-sensitive detector (PSD, Bruker). Phase quantification was performed using the Rietveld refinement method<sup>30</sup> employing the GSAS/EXPGUI software package.<sup>31</sup> Raman scattering spectra were acquired using a LabRAM HR Evolution spectrometer (Horiba) coupled to a confocal microscope with a He-Ne laser (632.8 nm) excitation source. Spectral data were collected in the 10-400 cm<sup>-1</sup> range, with a scan step width of 0.8 cm<sup>-1</sup>, utilizing a 100× objective lens for precise sample focusing. LabSpec 5 software (Horiba) was used for data acquisition. Diffuse Reflectance Spectroscopy (DRS) measurements were conducted using a Shimadzu UVvis-NIR spectrophotometer (UV 3600), covering the 250-800 nm range, with a scan step width of 0.5 nm. Barium sulfate (BaSO<sub>4</sub>) was used as the reference standard. Scanning electron micrographs of the powder samples were collected using a ZEISS LEO 440 microscope (Cambridge, England) equipped with an OXFORD model 7060 detector, operated with a 15 kV electron beam. Transmission Electron Microscopy (TEM) results were obtained using a JEOL JEM-2100 LaB6

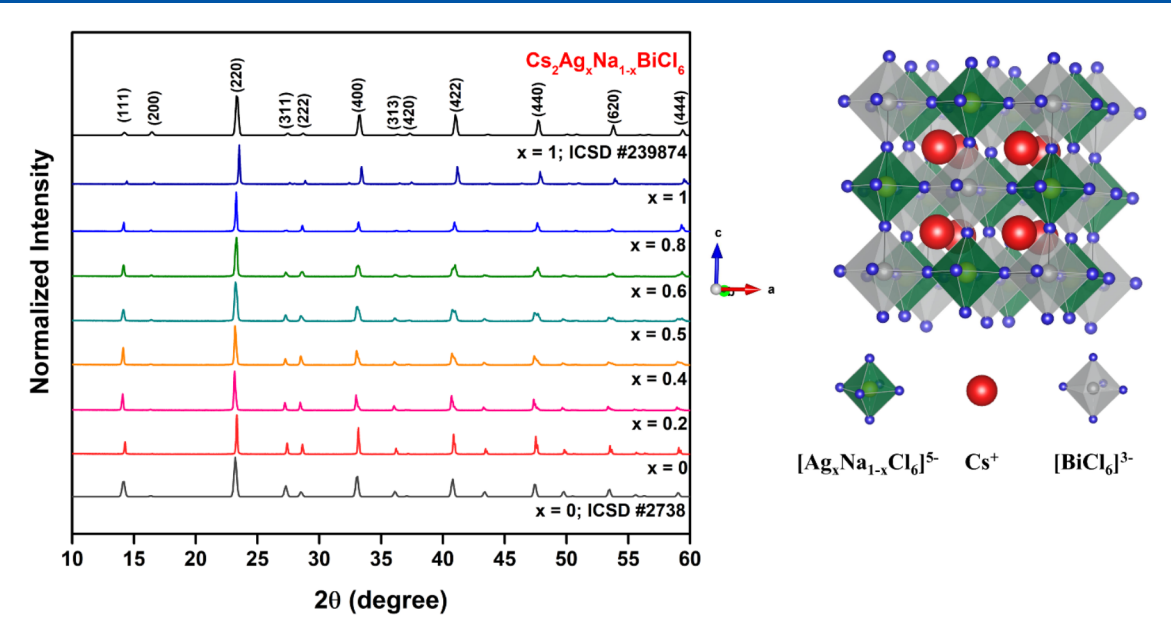


Figure 1. X-ray diffractograms of the obtained powders for the Cs<sub>2</sub>Ag<sub>x</sub>Na<sub>1-x</sub>BiCl<sub>6</sub> perovskite compositions.

microscope operating at 200 kV, coupled to an EDS system for elemental mapping. Samples were prepared on carbon-coated copper mini-grids (CFC-200Cu, Electron Microscopy Sciences). For visualization of the heterojunction between the AgCl and BiOCl semiconductors, dilute aqueous suspensions were used, while the perovskite, in its initial form, was analyzed from a suspension in HPLC-grade ethanol.

**2.4. Computational Details.** All double perovskites were investigated from periodic models based on the Fm3m space group, constructed from experimental data reported by Filip and co-workers.<sup>32</sup> To achieve an adequate Ag-loading level, similar to the experimental conditions, the bulk models were expanded to  $2 \times 2 \times 2$  supercells. The AgCl and BiOCl models were constructed in the  $Fm\overline{3}m$  and P4/nmm crystalline structures, respectively, as reported by Hull et al.<sup>33</sup> and Andrade et al.<sup>34</sup> The electronic properties were analyzed through the density of states (DOS), which provides insight into the atomic contributions of each chemical species to the valence band (VB) and conduction band (CB) edges. The band structure (BS) profiles, considering the same energy levels, were also evaluated. From the DOS and BS results, critical charge carrier characteristics were derived using the Fermi-Dirac distribution<sup>35,36</sup> and the effective mass method.<sup>37,38</sup>

All simulations were performed using a DFT/WC1LYP level of theory implemented in the CRYSTAL23<sup>39</sup> code package, under vacuum conditions and at 0 K. This hybrid exchange-correlation functional consists of a mixing of nonlocal HF and the Wu-Cohen GGA exchange with the Lee–Yang–Parr correlation (eq 1).<sup>40,41</sup> This level of theory was chosen taking into account the higher accuracy of electronic properties in comparison to B3LYP, PBE0, and HSE06, as demonstrated in Figure S1.

$$E_{\rm XC}[\rho] = aE_{\rm HF}^{x} + (1 - a)E_{\rm DFT}^{x} + E_{\rm DFT}^{C}$$
 (1)

Additional calculation criteria: The energy self-consistent field (SCF) convergence criteria were set to  $10^{-7}$  Hartree, and the Monkhorst–Pack grid was set to  $8\times8\times8$ . The Cs, Ag, and Bi atoms were described using the HAYWSC-31(1d)G, doll-ECP, and EPC60MDF pseudopotentials, respectively. The Na and

Cl atoms were represented by 8–511G and 86–311G Gaussian basis sets.

**2.5. Photocatalysis Assays.** For the photocatalytic assays, a 20 ppm aqueous solution of crystal violet (CV) was prepared. Then, 35 mg of the photocatalyst was dispersed in 35 mL of water using an ultrasonic bath for 30 min. Subsequently, 35 mL of the CV solution was transferred into a cylindrical borosilicate photoreactor and kept in the dark for 30 min under constant magnetic stirring to establish adsorption equilibrium. The photocatalytic process was initiated by illuminating the solution within the borosilicate reactor using a UV lamp (LightningCure, Hamamatsu, Japan) with an optical fiber positioned 6 cm from the reactor wall. Light intensities were as follows: UVA = 32.3 mW/cm<sup>2</sup> and visible light =  $30.8 \text{ mW/cm}^2$ . To monitor dye removal efficiency over time, aliquots of 1.5 mL were collected from the photoreactor outlet at different time intervals. The collected aliquots were centrifuged, and the supernatant was analyzed. The concentration of CV dye in the samples was determined by measuring the absorbance in the range of  $\lambda = 450-700$  nm using a USB 4000 spectrometer (Ocean Optics) The same procedure was followed for experiments conducted in alcoholic solutions, using HPLC-grade ethanol (Panreac) to prepare the solutions. Reusability tests were performed by conducting four successive cycles of CV dye photodegradation in aqueous media using the Ag<sub>1,0</sub> sample. After each cycle, the photocatalyst was recovered by centrifugation, washed with ethanol and deionized water, resuspended in deionized water, and reused in a new cycle with the addition of fresh CV solution, following the same photocatalytic procedure (light exposure for 60 min). Additional reusability experiments were also carried out by adding 1000  $\mu$ L of a 50% H<sub>2</sub>O<sub>2</sub> solution before each cycle, immediately prior to light irradiation.

# 3. RESULTS AND DISCUSSION

**3.1. Synthesis and Characterization.** The proposed experimental procedure successfully yielded pure and crystalline Bi-based perovskite samples, as evidenced by the well-defined and sharp diffraction peaks displayed in Figure 1. According to crystallographic reports on lead-free double

halide perovskites, these materials crystallize in a cubic crystal system with an  $Fm\overline{3}m$  space group and unit cell volume of 1251.65 Å<sup>3</sup>.<sup>42</sup> As observed in Figure 1, the diffraction pattern confirms the formation of Bi-based perovskite in a cubic phase, consistent with the reference patterns of Cs<sub>2</sub>AgBiCl<sub>6</sub>.

The characteristic diffraction peaks corresponding to the (111), (200), (220), (311), (222), (400), (313), (420), (422), (440), (620), and (440) planes confirm the formation of Bibased perovskites. 42,43 A gradual decrease in the (200) peak intensity and a simultaneous increase in the (111) peak indicate the progressive incorporation of Na+, shifting the composition toward Cs<sub>2</sub>NaBiCl<sub>6</sub>. This trend is further supported by the behavior of the (311) and (222) peaks, which become more prominent as the Ag<sup>+</sup> content decreases, consistent with previously reported XRD data. The XRD patterns of  $Cs_2Ag_xNa_{1-x}BiCl_6$  samples thus confirm the successful formation of Ag<sup>+</sup>/Na<sup>+</sup>-mixed perovskite. Additionally, a gradual transition from off-white to yellowish is observed as the Ag+ content increases (Figure S2), which can be attributed to modifications in the bandgap values. The crystallite size was estimated using the Debye-Scherrer equation applied to the most intense reflections, namely (220), (400), and (422), as presented in Table S1. Samples located at the extremes of composition (Ag1.0, Ag0.8, Ag0.2 and Ag0.0) exhibit larger crystallite sizes (50-60 nm), while the intermediate mixed compositions present smaller average sizes (28-36 nm). This trend suggests that partial substitution of Ag and Na ions introduces lattice distortion and local strain, which hinders crystal growth and results in reduced crystallite size. In contrast, the pure endmembers crystallize with fewer distortions, favoring larger crystallite sizes. Moreover, scanning electron microscopy (SEM) micrographs (Figure S3) revealed that the powders are composed of particles predominantly in the micrometer range, exhibiting a broad size distribution. In all cases, larger particles were surrounded by smaller ones, with the former displaying well-defined octahedral morphology. This combination of particle size distribution and octahedral shape was consistently observed across all synthesized samples.

Raman spectroscopy was performed to investigate the structural characteristics of the Bi-based perovskites. As shown in Figure 2, the Raman spectra of the synthesized samples exhibit three distinct vibrational modes below 400 cm<sup>-1</sup>, attributed to the vibrational modes of AgCl<sub>6</sub> and BiCl<sub>6</sub> octahedra. 44,45 The band centered at 115 cm<sup>-1</sup> is assigned to the bending vibration of Ag-Cl and Bi-Cl bonds, exhibiting T<sub>2g</sub> symmetry. The Bi-Cl bonds play a dominant role in this vibrational mode, as indicated by a slight shift in the 115 cm<sup>-1</sup> band with decreasing Ag content. The band at 213 cm<sup>-1</sup> corresponds to the  $E_g$  vibrational mode of the  $AgCl_6$ octahedron, while the band at 282 cm<sup>-1</sup> is associated with the A<sub>1g</sub> stretching vibrations of both AgCl<sub>6</sub> and BiCl<sub>6</sub> octahedra. As observed in Figure 2, all vibrational bands exhibit a gradual shift to lower wavenumber with decreasing Ag+ concentration. This trend indicates that Ag+ substitution affects the Eg and Alg vibrational modes, leading to a progressive tuning of both bands. For instance, the  $T_{2g}$  mode at 115 cm<sup>-1</sup> shifts from 115 cm<sup>-1</sup> ( $Ag_{1.0}$ ) to 112 cm<sup>-1</sup> ( $Ag_{0.0}$ ), while the  $A_{1g}$  mode at 281 cm<sup>-1</sup>, shifts from 281 cm<sup>-1</sup> ( $Ag_{1.0}$ ) to 278 cm<sup>-1</sup> ( $Ag_{0.0}$ ). This decrease in phonon energy suggests that Ag content plays a critical role in the vibrational dynamics of the perovskite lattice.

Additionally, it is evident that the full width at half-maximum (FWHM) of the Raman bands increases with the

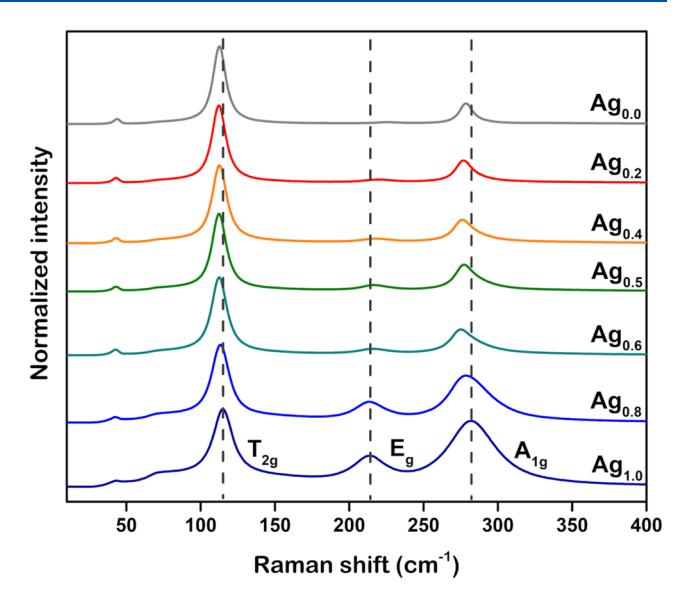


**Figure 2.** Raman spectra of  $Cs_2Ag_{x}Na_{1-x}BiCl_6$  double perovskites with varying  $Ag^+$  concentrations (x=0.0 to 1.0). The spectra exhibit three distinct vibrational modes below 400 cm<sup>-1</sup>, assigned to  $T_{2g}$  (bending vibration at ~115 cm<sup>-1</sup>),  $E_g$  (~213 cm<sup>-1</sup>), and  $A_{1g}$  (stretching vibration at ~282 cm<sup>-1</sup>) modes, corresponding to the vibrational dynamics of  $AgCl_6$  and  $BiCl_6$  octahedra. As the  $Ag^+$  content increases, a progressive shift to lower wavenumbers is observed, along with broadening of the bands, indicating modifications in the perovskite lattice due to  $Ag^+$  substitution.

Ag<sup>+</sup> content, indicating greater structural disorder and phonon scattering. This broadening can be attributed to multiple factors. First, the difference in the polarization strength between Ag+ and Na+ significantly influences the lattice dynamics. Ag+ has a higher polarizing power due to its higher effective nuclear charge and higher charge density compared to Na<sup>+</sup>. Consequently, Ag<sup>+</sup> ions introduce stronger local distortions in the lattice, increasing the vibrational mode anharmonicity and leading to broader Raman peaks. 46 Second, the introduction of Ag+ into the lattice increases site heterogeneity and defect formation. The larger ionic radius of Ag+ compared to Na+ causes strain in the crystal lattice, leading to local structural disorder. Such disorder contributes to an increased distribution of phonon states, which in turn results in a broadened Raman signal. Furthermore, as demonstrated in previous studies on Raman peak shift and broadening in crystalline nanoparticles with lattice impurities, the presence of dopants and vacancies modifies the local vibrational environment, leading to increased phonon scattering and a more pronounced line width broadening.<sup>4</sup>

The optical bandgap for each composition was determined using the Tauc plot method, as described in Makula's work. Diffuse reflectance spectroscopy (DRS) data (Figure S4) was collected and analyzed to extract the bandgap values using eq 1, where  $F(R\infty)$  represents the Kubelka–Munk function, h is Planck's constant,  $\nu$  is the photon frequency,  $E_{\rm gap}$  is the bandgap energy, B is a constant, and  $\gamma$  is a parameter dependent on the nature of the electronic transition,  $\gamma=1/2$  for direct bandgaps and  $\gamma=2$  for indirect bandgaps. All measured bandgap values are listed in Table 1. The Ag<sub>1.0</sub> sample exhibited an indirect bandgap of 2.70 eV, which is in reasonable agreement with previously reported values (2.84 eV). Likewise, the Ag<sub>0.0</sub> sample presented a bandgap of 3.49 eV, consistent with literature reports. However, the values

Table 1. Calculated Bandgaps of Cs<sub>2</sub>Ag<sub>x</sub>Na<sub>1-x</sub>BiCl<sub>6</sub> Perovskites by Using Tauc Plot Method

chemical composition	sample label	bandgap ±0.03 (eV)
Cs <sub>2</sub> AgBiCl <sub>6</sub>	$Ag_{1.0}$	2.70
$Cs_2Ag_{0.8}Na_{0.2}BiCl_6$	$Ag_{0.8}$	2.50
Cs <sub>2</sub> Ag <sub>0.6</sub> Na <sub>0.4</sub> BiCl <sub>6</sub>	$Ag_{0.6}$	2.51
Cs <sub>2</sub> Ag <sub>0.5</sub> Na <sub>0.5</sub> BiCl <sub>6</sub>	$Ag_{0.5}$	2.52
$Cs_2Ag_{0.4}Na_{0.6}BiCl_6$	$Ag_{0.4}$	2.49
$Cs_2Ag_{0.2}Na_{0.8}BiCl_6$	$Ag_{0.2}$	2.49
Cs <sub>2</sub> NaBiCl <sub>6</sub>	$Ag_{0.0}$	3.33

obtained in this study are slightly lower than the reported literature values, which can be attributed to differences in synthesis conditions, such as the pH of the reaction medium, a well-known factor influencing the bandgap of semiconductors. Additionally, double perovskites with intermediate  $Ag^+$  concentrations exhibited similar bandgap values, suggesting that the  $Ag^+/Na^+$  ratio has a subtle impact on the optical properties within this compositional range.

$$(F(R\infty)h\nu)^{1/\gamma} = B(h\nu - E_{\rm gap})$$
(2)

3.2. Electronic Structure Analysis via DFT. As previously mentioned, the electronic structures of Cs<sub>2</sub>Ag<sub>x</sub>Na<sub>1-x</sub>BiCl<sub>6</sub> perovskites was investigated through DOS and BS analyses. The calculated DOS results (Figure 3) indicate that Bi ions significantly contribute to the formation of the valence bands (VB) and are the primary contributors to the conduction bands (CB) energy levels. In contrast, Cl<sup>-</sup> species exhibit the opposite behavior, with a reduced contribution to the CB and a pronounced presence in the VB. The Cs<sup>+</sup> and Na<sup>+</sup> ions do not play a significant role in the formation of either band within the evaluated energy range. Meanwhile, the Ag<sup>+</sup> species contribute similarly to both the VB and CB, with the Ag and Cl contributions becoming comparable as the Ag<sup>+</sup> content increases. Regarding BS analysis (Figure 3), all investigated double perovskites exhibit direct bandgaps at the  $\Gamma$ - $\Gamma$  (GM-GM) points. The materials with intermediate Ag<sup>+</sup> concentrations within the double perovskite structure present a wider energy separation between the VB and CB levels compared to Cs2NaBiCl6 and Cs2AgBiCl6. Notably, certain energy levels in Cs<sub>2</sub>NaBiCl<sub>6</sub>, Cs<sub>2</sub>Ag<sub>0.12</sub>Na<sub>0.87</sub>BiCl<sub>6</sub>, and Cs<sub>2</sub>Ag<sub>0.25</sub>Na<sub>0.75</sub>BiCl<sub>6</sub> exhibit flat band behavior, suggesting that these states are minimally influenced by high-symmetry points in the Brillouin zone.

DOS analysis in solid-state materials also allows for the estimation of charge carrier concentration and the temperature influence on electron—hole pair dynamics via Fermi—Dirac distribution analysis. This enables the prediction of the semiconductor type, where a higher hole (h<sup>+</sup>) concentration suggests a p-type semiconductor, while an increased electron (e<sup>-</sup>) concentration indicates an n-type behavior. As displayed in Table 2, the calculated values suggest that all investigated materials exhibit n-type semiconductor behavior. Furthermore, charge carrier concentration values at 300, 600, and 900 K demonstrate a significant increase with rising temperature, as expected for semiconductors.

The effective mass method applied to BS results provides valuable insights into charge carrier stability and photocatalytic potential. By interpolating the maximum and minimum points of the VB and CB, the effective masses of electrons  $\left(\frac{m_e^*}{n_c}\right)$  and

 $\frac{m_{\text{h}^*}}{m}$  were determined. As widely reported in the literature, materials where electrons and holes have similar effective masses tend to exhibit higher recombination rates, limiting charge carrier lifetimes and reducing photocatalytic efficiency. Conversely, a significant disparity in effective masses, typically characterized by an electron-to-hole mass ratio  $\left(\frac{m_{h^*}}{m_{h^*}}\right)$  lower than 0.5 or higher than 1.5, promotes spatial charge separation, reducing electron-hole recombination and potentially enhancing photocatalytic activity. 37,38,50,51 It should be noted, however, that photocatalytic efficiency is also influenced by other critical factors, including band edge alignment with redox potentials, defect states, and surface interactions with reactants. Therefore, while a comprehensive assessment of the electronic structure and material properties is essential to accurately explain photocatalytic performance, the effective mass ratio remains an important indicator of charge transport and recombination, potentially offering valuable insights into the optimal electronic properties for photocatalytic applications.

As shown in Table 3,  $Cs_2Ag_xNa_{1-x}BiCl_6$  perovskites with Ag concentrations between 0.25 and 0.62 exhibit the most favorable combination of electronic properties for photocatalysis. Their bandgap values (2.59–2.68 eV) fall within the optimal range for visible-light activation, while their effective mass ratios  $\left(\frac{m_{h^*}}{m_{e^*}}\approx 1.5-1.7\right)$  indicate efficient charge separation with reduced recombination rates. In contrast, perovskites with higher  $Ag^+$  content (x>0.75) show lower charge carrier stability, leading to increased electron—hole recombination and, consequently, diminished photocatalytic performance. On the other hand,  $Na^+$ -rich perovskites ( $Ag_{0.0}$  and  $Cs_2Ag_{0.12}Na_{0.87}BiCl_6$ ) exhibit large bandgaps (>3.3 eV), restricting their absorption to the UV region and limiting their efficiency under visible light irradiation.

Finally, the DFT-predicted bandgap values confirm that all  $Cs_2Ag_xNa_{1-x}BiCl_6$  perovskites exhibit bandgaps within the expected range for semiconductors, demonstrating remarkable consistency with experimental data. As depicted in Figure 4, the close alignment between theoretical and experimental values underscores the reliability of DFT calculations in accurately capturing the electronic properties of these materials. Notably, moderate  $Ag^+$  substitution  $(0.25 \le x \le 0.62)$  emerges as the key factor in achieving an optimal balance between bandgap reduction, efficient charge carrier separation, and suppressed recombination, thereby positioning these compositions as promising candidates for visible-light-driven photocatalysis.

**3.3. Photocatalytic Activity Behavior.** The photocatalytic performance of the investigated perovskite materials was assessed through the photodegradation of crystal violet (CV) dye in both aqueous and ethanolic solutions (Figure 5). The use of these two distinct media was motivated by the reported stability of Cs<sub>2</sub>AgBiCl<sub>6</sub> photocatalysts in ethanol<sup>27</sup> and the need to evaluate their efficiency in a more relevant environment for contaminant degradation. Furthermore, these results provide insights into the potential decomposition mechanisms of Ag/Bi metal-halide double perovskites under such conditions. The photocatalytic degradation profiles of Ag/Bi metal-halide double perovskites in aqueous media (Figure 5a) exhibit an exponential decay that is well described by pseudo-first-order kinetics (Figures 5c and S5). This kinetic

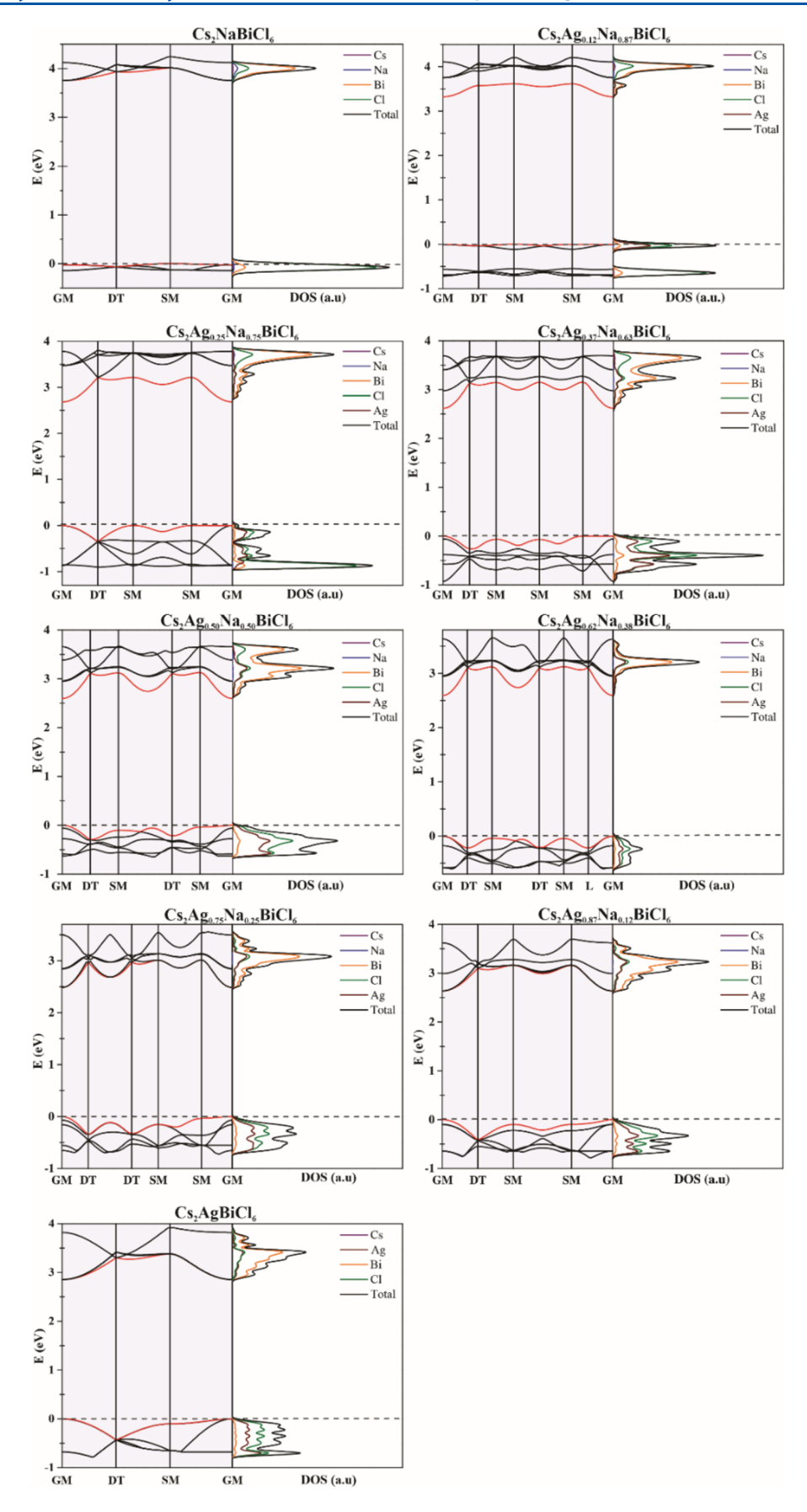


Figure 3. Projected density of states (DOS) and band structures (BS) for  $Cs_2Ag_xNa_{1-x}BiCl_6$  perovskites. The band structure analysis was performed along high-symmetry points of the Brillouin zone, which are GM (0.0 0.0 0.0), DT (0.5 0.0 0.0), (0.0 0.0 0.5), SM (0.5 0.5 0.0), (0.5 0.0 0.0)

Figure 3. continued

0.5), and L (0.5 0.5 0). The DOS plots illustrate the contributions of Cs, Na, Ag, Bi, and Cl atoms to the electronic states. The evolution of the electronic band structure with varying Ag content highlights the effect of cation substitution on the perovskite's optical and electronic properties.

Table 2. Charge Carrier Density (cm<sup>-3</sup>) at 300, 600, and 900 K Obtained from Fermi–Dirac Distribution for the  $Cs_2Ag_xNa_{1-x}BiCl_6$  Materials

			charge carrier den	sity (×10 <sup>18</sup> cm <sup>-3</sup> )		
	300 K		600 K		900 K	
materials	h <sup>+</sup>	e <sup>-</sup>	h <sup>+</sup>	e <sup>-</sup>	h <sup>+</sup>	e <sup>-</sup>
Ag <sub>0.0</sub>	3.049	4.966	3.125	5.089	3.312	5.394
$Cs_2Ag_{0.12}Na_{0.87}BiCl_6$	1.494	3.844	1.531	3.940	1.622	4.175
Cs <sub>2</sub> Ag <sub>0.25</sub> Na <sub>0.75</sub> BiCl <sub>6</sub>	1.869	3.027	1.915	3.102	2.030	3.288
Cs <sub>2</sub> Ag <sub>0.37</sub> Na <sub>0.63</sub> BiCl <sub>6</sub>	0.861	2.613	0.882	2.677	0.935	2.838
$Cs_2Ag_{0.50}Na_{0.50}BiCl_6$	0.625	2.598	0.640	2.663	0.679	2.822
Cs <sub>2</sub> Ag <sub>0.62</sub> Na <sub>0.38</sub> BiCl <sub>6</sub>	0.561	3.732	0.575	3.825	0.609	4.054
Cs <sub>2</sub> Ag <sub>0.75</sub> Na <sub>0.25</sub> BiCl <sub>6</sub>	0.509	2.232	0.522	2.881	0.553	2.424
Cs <sub>2</sub> Ag <sub>0.87</sub> Na <sub>0.12</sub> BiCl <sub>6</sub>	0.452	2.493	0.463	2.555	0.490	2.708
$Ag_{1.0}$	0.507	2.203	0.520	2.258	0.551	2.393

Table 3. Bandgap (eV) and Effective Masses for the Charge Carriers of the Cs<sub>2</sub>Ag<sub>x</sub>Na<sub>1-x</sub>BiCl<sub>6</sub> Materials

		effective mass			
materials	band gap energies (eV)	$\frac{m_{\text{h}^*}}{m_{\text{o}}}$	$\frac{m_{\rm e}*}{m_{\rm o}}$	$\frac{m_{\text{h}^*}}{m_{\text{e}^*}}$	
$Ag_{0.0}$	3.75	1.6549	0.2927	5.6546	
$Cs_2Ag_{0.12}Na_{0.87}BiCl_6$	3.32	0.8959	0.1464	6.1182	
$Cs_2Ag_{0.25}Na_{0.75}BiCl_6$	2.68	0.1550	0.1011	1.5327	
$Cs_2Ag_{0.37}Na_{0.63}BiCl_6$	2.61	0.1672	0.1020	1.6394	
$Cs_2Ag_{0.50}Na_{0.50}BiCl_6$	2.59	0.1681	0.1021	1.6469	
$Cs_2Ag_{0.62}Na_{0.38}BiCl_6$	2.59	0.1744	0.1027	1.6979	
$Cs_2Ag_{0.75}Na_{0.25}BiCl_6$	2.48	0.1457	0.1080	1.3488	
$Cs_2Ag_{0.87}Na_{0.12}BiCl_6$	2.63	0.1329	0.1046	1.2705	
$Ag_{1.0}$	2.85	0.1318	0.1038	1.2701	

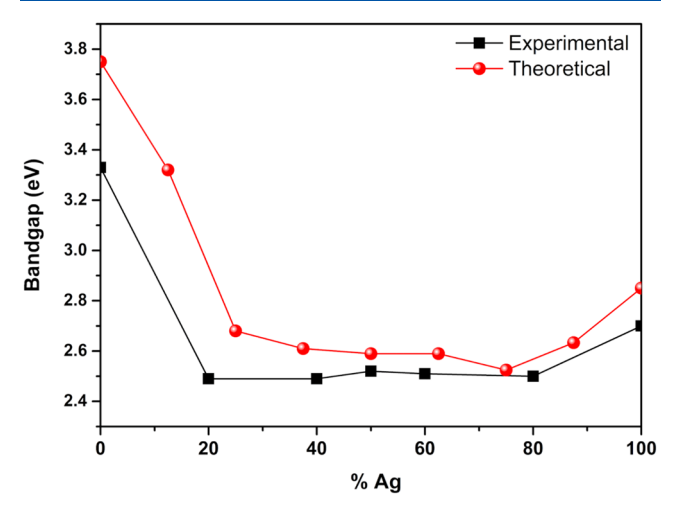


Figure 4. Comparison between theoretical and experimental band gap values obtained for  $Cs_2Ag_xNa_{1-x}BiCl_6$  perovskites.

model is conventionally employed to analyze photocatalytic dye degradation experiments and allows for the determination of observed kinetic constants  $(k_{\rm obs})$ , facilitating a comparative analysis of photocatalytic efficiency in aqueous solutions (Figure 5e).

In contrast, photocatalytic experiments in ethanolic media exhibit a more complex kinetic behavior (Figure 5b). A 10-20 min induction period is observed before significant dye degradation occurs, after which the kinetics become linear. As shown in Figures 5d and S6, this latter phase is well-fitted into a pseudozero-order model. The induction period may be attributed to surface activation of the photocatalyst, degradation of adsorbed solvent molecules, or changes in reaction intermediates under ethanolic conditions. A similar pseudozero-order kinetic behavior has been reported for the photocatalytic degradation of various dyes using Cs<sub>2</sub>AgBiBr<sub>6</sub> double perovskite photocatalysts in ethanolic media. 52 Although the exact mechanisms underlying this complex behavior remain uncertain, the pseudozero-order model fitting of the linear decay regime was employed to estimate and compare the photocatalytic performance of the materials in ethanolic solutions (Figure 5f).

A comparison of the  $k_{\rm obs}$  values determined in aqueous (Figure 5e) and ethanolic (Figure 5f) media reveals that the influence of chemical composition on photocatalytic activity occurs in contrasting ways depending on the medium. This behavior highlights the central role of Ag concentration in this phenomenon. For photocatalytic CV dye degradation assays in aqueous solution, an increase in Ag content leads to a significant and gradual enhancement of photocatalytic activity. Notably, the  $k_{\text{obs}}$  value for the Ag<sub>1.0</sub> sample (Cs<sub>2</sub>AgBiCl<sub>6</sub>) is 5.6 times higher than that found for the Ag<sub>0.0</sub> sample (Cs<sub>2</sub>NaBiCl<sub>6</sub>). However, an opposite trend is observed in ethanolic media, where photocatalytic activity decreases as Ag content increases. In this case, the Ag<sub>0.0</sub> sample exhibits a  $k_{\rm obs}$ value 2.6 times higher than the Ag<sub>1.0</sub> sample. These contrasting behaviors can be attributed to the different structural stabilities of the prepared perovskites in aqueous and ethanolic media. According to Guo et al., 27 Ag/Bi metal-halide double perovskites retain their structure after photocatalytic experiments in ethanolic media, aside from minor formation of metallic Ag, as confirmed by XRD results (Figure S7). Thus, under such conditions, the intrinsic photocatalytic activity of the investigated perovskite structures can be assessed. Thus, under such conditions, the intrinsic photocatalytic activity of the investigated perovskite structures can be assessed. The

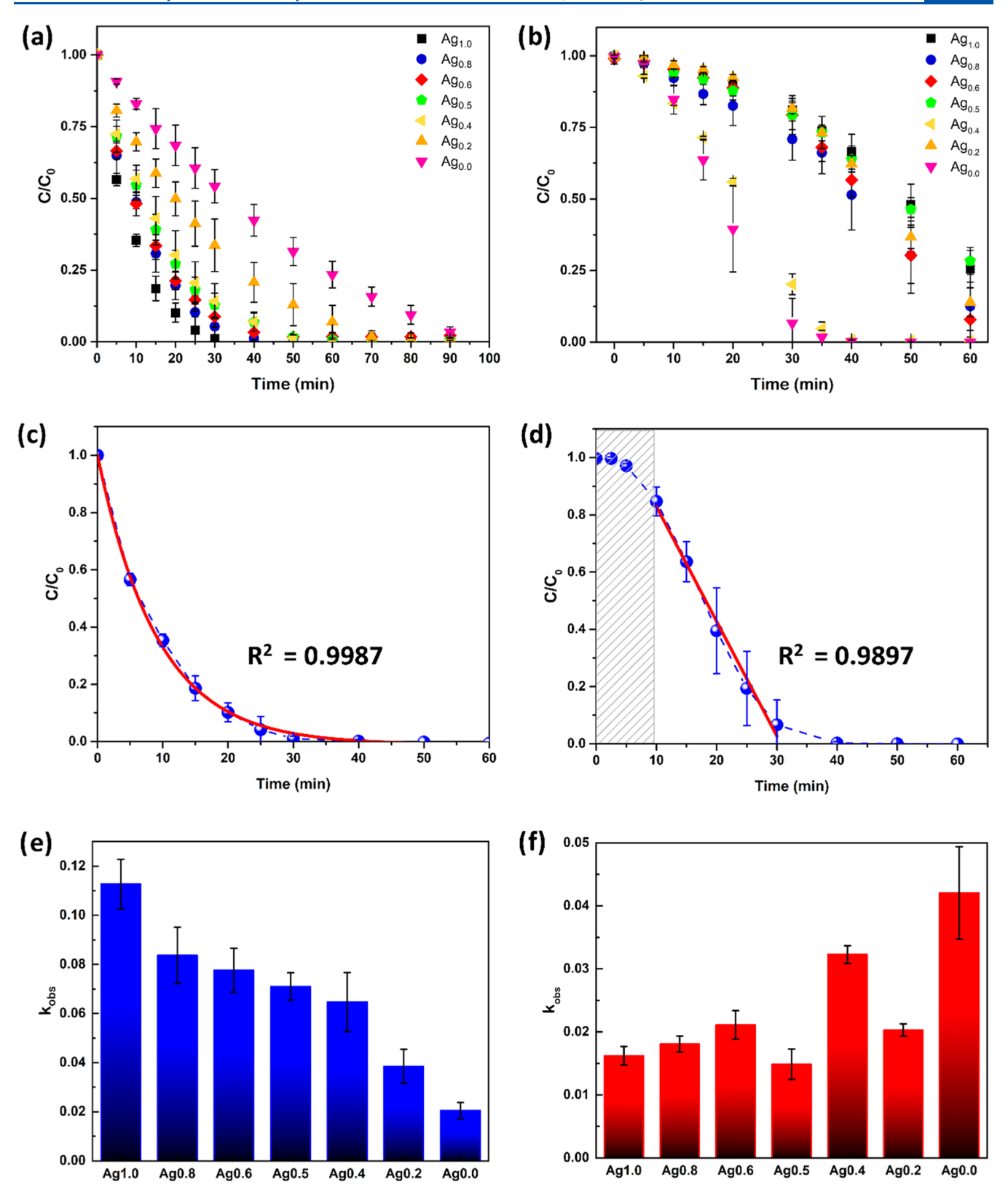


Figure 5. Photocatalytic CV dye degradation kinetic profiles using the  $Cs_2Ag_xNa_{1-x}BiCl_6$  perovskite photocatalysts in (a) aqueous and (b) ethanolic media. (c) Representative exponential decay with pseudo-first-order kinetic fitting for photocatalytic experiments in aqueous media (sample Ag1.0). (d) Representative complex kinetic behavior in ethanolic media (sample Ag0.0) showing an initial induction period (gray shaded area) followed by a linear decay fitted to a pseudozero-order model. Comparison of (e) pseudo-first order observed kinetic constants ( $k_{obs}$ ) in aqueous media. and (f) pseudozero-order observed kinetic constants in ethanolic media for the different  $Cs_2Ag_xNa_{1-x}BiCl_6$  perovskite photocatalysts.

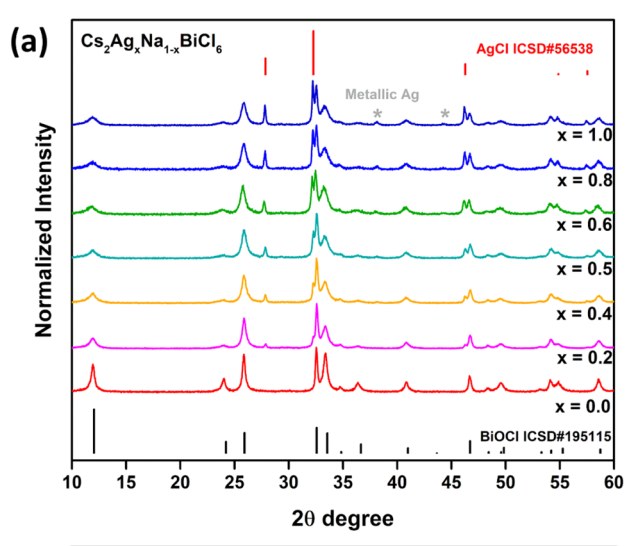
observed behavior can be rationalized by the structural, vibrational, optical, and electronic properties of the prepared double perovskite materials. Structural analyses (XRD, Raman, and DRS) confirmed the formation of single-phase double perovskites with systematic compositional changes that directly affect charge-carrier properties, as also supported by DFT results. Indeed, the experimental trend aligns with the theoretical DFT predictions, as the calculated charge-carrier recombination rates (evaluated from effective masses, Table 4)

Table 4. Percentage of BiOCl, AgCl, and Ag Phases Obtained from Each Proposed Double Perovskite Material in after Photocatalytic Run Aqueous Media

samples	BiOCl (%)	AgCl(%)	Ag (%)	R <sub>wp</sub> (%)	GOF
Ag1.0	72.9	24.4	2.7	8.92	1.264
Ag0.8	76.5	21.1	2.4	11.11	1.162
Ag0.6	77.7	20.6	1.6	10.02	1.149
Ag0.5	79.2	19.9	0.9	9.25	1.313
Ag0.4	84.6	14.5	0.9	8.42	1.305
Ag0.2	92.3	7.7	-	8.44	1.336
Ag0.0	100	-	-	10.56	1.428

suggest a decrease in photocatalytic efficiency with increasing Ag content. Moreover, Raman spectroscopy revealed that Agrich compositions exhibit peak broadening and frequency shifts, indicative of lattice disorder, which may promote nonradiative recombination and further explain the reduced activity of Ag-rich samples in ethanol, where the perovskite structure remains stable. Finally, although DRS and DFT analyses indicate that increasing Ag content narrows the bandgap and extends absorption into the visible region, these beneficial light-harvesting properties are counterbalanced by faster recombination, resulting in lower overall efficiency

Conversely, Ag/Bi metal-halide double perovskites underwent complete decomposition in aqueous media, forming predominantly BiOCl and AgCl, as evidenced by XRD data (Figure 6a). Phase quantification analysis was performed for all samples using Rietveld refinement, allowing for a quantitative assessment of the phase formation after photocatalytic experiments in aqueous media. Figure 6b presents the refined XRD data for the Ag<sub>1.0</sub> sample (data for all samples are provided in Figure S8). Table 4 summarizes the phase fractions determined by Rietveld refinement, along with the  $R_{\rm wp}$  and GOF statistical parameters. The relatively low  $R_{\rm wp}$  values (<10%) and  $\chi^2$  values (<1.5) observed in most refinements indicate a good agreement between the experimental and calculated data. These values, combined with the qualitative assessment of the refinement residual graphs (Figure S8), confirm the adequacy of the proposed model and demonstrate the reliability of the refinement analysis.<sup>53</sup> Formation of BiOCl and AgCl is further corroborated by TEM and EDS mapping for the Cs<sub>2</sub>AgBiCl<sub>6</sub> (Ag1.0 sample) sample after exposure to ethanolic and aqueous media, as shown in Figure 7. TEM images and EDS mapping of the perovskite after exposure to ethanol confirm the preservation of a single-phase material with micrometer-sized particles and a homogeneous distribution of the constituent elements. In contrast, after exposure to aqueous media, a different outcome is observed: TEM images reveal the formation of nanocrystals of varying sizes, while EDS analysis indicates a heterogeneous distribution of Ag and Bi across different regions. These results further support the



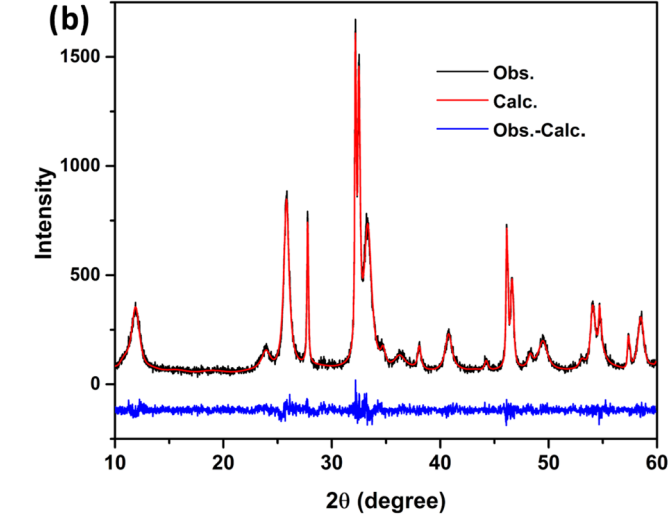


**Figure 6.** (a) X-ray diffractograms of  $Cs_2Ag_xNa_{1-x}BiCl_6$  after the photocatalysis run in aqueous media. (b) Rietveld refinement plot for sample Ag1.0 after the photocatalytic run.

decomposition of the perovskite into agglomerated AgCl and BiOCl nanocrystals in close contact.

Phase quantification data reveals a reasonably expected trend: the percentage of BiOCl generated increases progressively from Ag<sub>1.0</sub> to Ag<sub>0.0</sub>, while the percentages of AgCl and metallic Ag decrease correspondingly. The increase in Ag content is also associated with the minor formation of metallic Ag, probably due to a photocorrosion process (photoinduced reduction of Ag+ ions). XRD and Rietveld analysis provide valuable insights into photocatalytic activity trends in aqueous media, suggesting that under these conditions, the photocatalytic properties observed refer to BiOCl, AgCl/BiOCl, or Ag/AgCl/BiOCl photocatalytic systems. Both BiOCl and AgCl are well-known semiconductors with significant photocatalytic activity reported in the literature. \$4,55 Additionally, the formation of an AgCl/BiOCl or Ag/AgCl/BiOCl electronic heterojunctions have been previously reported to enhance photocatalytic activity due to enhanced charge separation in the semiconductors interface. <sup>56,57</sup> To better understand the electronic profile of the expected heterojunction, DFT calculations for the AgCl and BiOCl materials were carefully performed (Supporting Information, Figure S9, Tables S2 and S3). The mismatch between the electronic levels of both

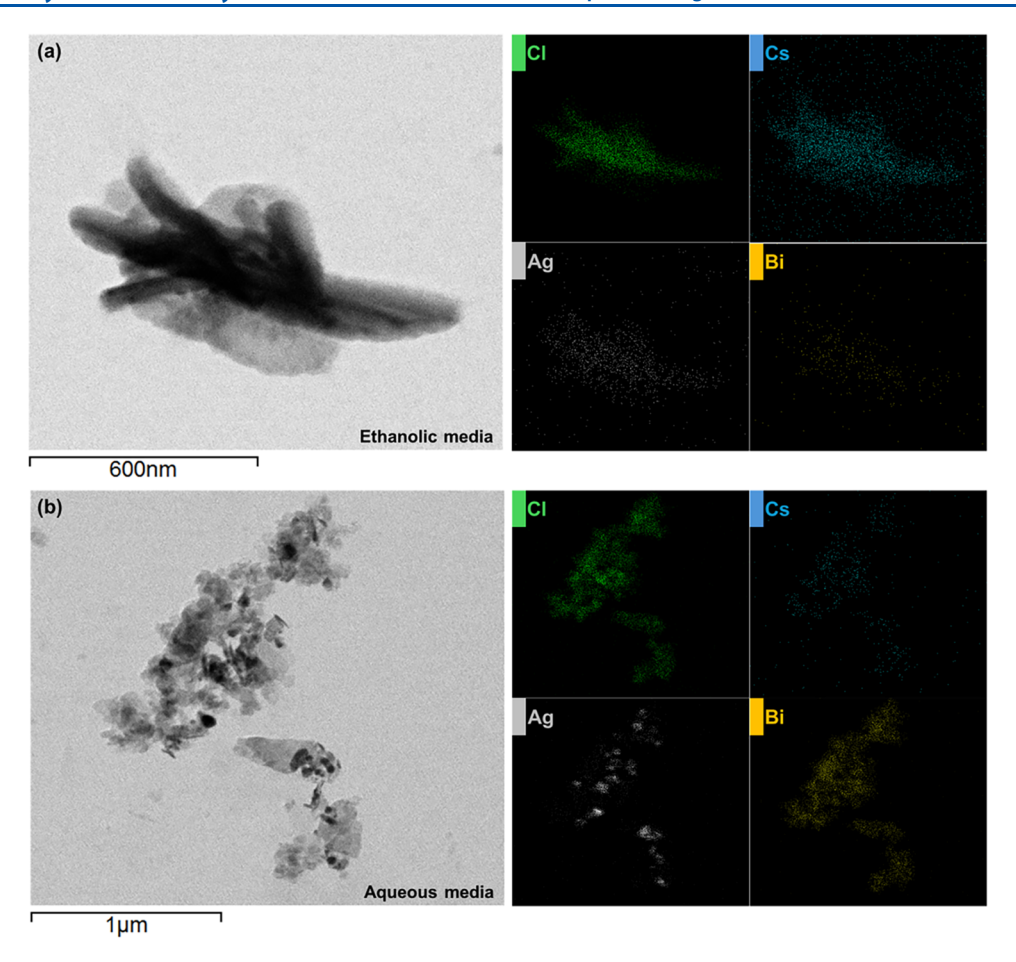


Figure 7. TEM images and EDS mapping for Cl, Cs, Ag, and Bi of the Ag1.0 sample after exposure to (a) ethanolic and (b) aqueous media.

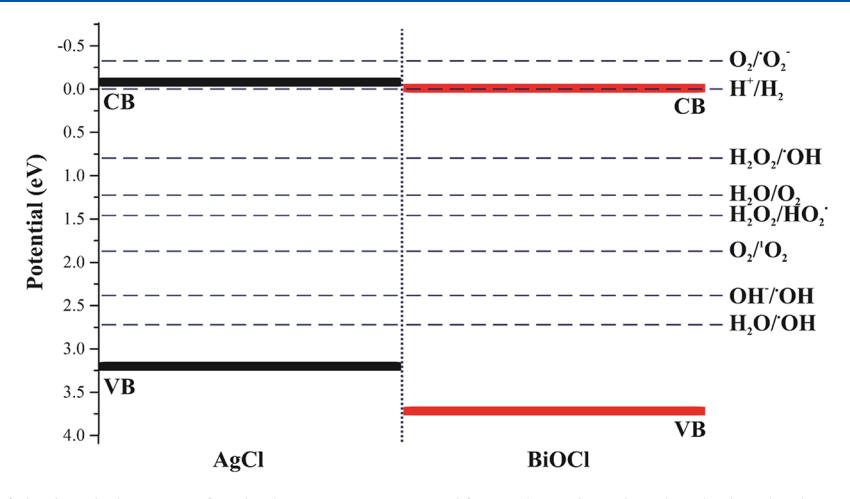


Figure 8. Schematic plot of the band alignment for the heterojunction AgCl/BiOCl combined with calculated valence and conduction band edge potential concerning the Hydrogen electrode potential (NHE) and vacuum.

materials was evaluated from the VB and CB band edge potentials calculated from a well-known set of equations. 58,59 As observed in Figure 8, the results indicate a type-II heterojunction. In this junction type, the charge carriers are found in both semiconductors, decreasing the recombination rate of the electron—hole pair. An additional analysis to better understand the photocatalytic activity of the investigated materials lies in the materials' ability to form reactive oxygen species (ROS) through surface reactions. It is possible to infer this from the comparison between the formation potential of

different ROS<sup>60</sup> and the band edge potential of the material. In the diagram obtained, as shown in the background of the heterojunction scheme (Figure 8), a negative CB edge potential evidence that the semiconductor is able to donate electrons, reducing species adsorbed on the surface. Meanwhile, positive VB edge potentials demonstrate that the materials surface can receive such adsorbed molecules, which will be oxidized. Therefore, the species whose formation potential was found within the CB and CB edge potentials can be formed on the materials surface. For the investigations, the

results evidence that the \*OH, HO<sub>2</sub>\*, and <sup>1</sup>O<sub>2</sub> radicals can be formed during a photocatalytic process. It is important to highlight that the formation of this species is strongly connected to the materials capacity to degrade persistent organic pollutants due to their high oxidizing power and reactivity. <sup>61,62</sup> Thereby, the calculated results shed light on the photocatalytic mechanism related to material employment. In addition, is particularly noteworthy the possibility of the formation of hydroxyl radicals, a fundamental species for the degradation of crystal violet, as already demonstrated in other studies. <sup>63,64</sup>

In summary, an improvement in the photocatalytic activity is expected for AgCl/BiOCl heterostructure in comparison to the isolated materials. Thus, the increased activity in aqueous media associated with the increase in Ag content may be explained by the in situ formation of AgCl/BiOCl heterojunctions, which exhibit enhanced photocatalytic activity compared to pure BiOCl, the sole degradation component of the Ag-free Cs<sub>2</sub>NaBiCl<sub>6</sub> perovskite (Sample Ag<sub>0.0</sub>). Moreover, the in situ formation of metallic silver (Ag0) during the photocatalytic process suggests the generation of a Schottky barrier at the Ag/AgCl and Ag/BiOCl interfaces. This phenomenon occurs because Ag<sup>0</sup> has a Fermi level lower than the conduction bands (CB) of AgCl and BiOCl, facilitating the extraction of photogenerated electrons from the semiconductors to the metallic surface. Therefore, the formation of Ag/AgCl/BiOCl heterostructures coupled with the Schottky barrier may also play a role in the enhanced photocatalytic activity observed with increasing Ag content in the samples. These findings confirm that the aqueous-phase decomposition of the perovskite can be strategically exploited to generate highly active interfaces, providing a synergistic effect between charge separation and redox reaction enhancement.

Nevertheless, the photoinduced extensive formation of metallic silver on silver-based semiconductors is known to deactivate the photocatalytic surface, leading to a loss of activity upon reuse. To evaluate the reusability of the metal halide double perovskite-derived AgCl/BiOCl heterojunction, the Ag1.0 sample was subjected to four successive cycles of CV dye photodegradation in aqueous media (Figure S10). As expected, a progressive and significant decrease in photocatalytic performance was observed, which can be attributed to surface deactivation caused by the accumulation of metallic Ag, which is consistent with previous reports for silver-based photocatalysts such as AgCl and Ag<sub>3</sub>PO<sub>4</sub>. <sup>54,65,66</sup> One possible strategy to avoid this silver-based photocorrosion process (Ag+ photoinduced reduction) is to conduct photocatalytic assays in the presence of H<sub>2</sub>O<sub>2</sub> as an auxiliary oxidant. Serge-Correales et al. 65 demonstrated that H<sub>2</sub>O<sub>2</sub> suppresses excessive metallic silver formation via a Fenton-like mechanism, where Ag<sup>0</sup> is reoxidized back to Ag+. In agreement with this report, we observed that in the presence of H2O2, the Ag1.0 sample maintained over 99% dye removal efficiency for four consecutive cycles (Figure S11), indicating that this approach effectively mitigates photocorrosion and extends the reusability of perovskite derived Ag-based heterojunction photocatalysts.

#### 4. CONCLUSIONS

In this study, we report on the preparation of lead-free double perovskites  $Cs_2Ag_xNa_{1-x}BiCl_6$  with varying Ag/Na content via a facile wet chemical route, as confirmed by XRD and Raman spectroscopy. DFT simulations were employed to describe the

electronic structure of this material series and its dependence on chemical composition. DFT-derived bandgap energies showed good agreement with experimental values and accurately predicted compositional trends. Additionally, charge carrier effective mass analysis suggests that increasing Ag content reduces photocatalytic efficiency due to enhanced charge carrier recombination. A key finding of this work is the significant impact of Ag/Na content on the photocatalytic activity of Cs<sub>2</sub>Ag<sub>2</sub>Na<sub>1-x</sub>BiCl<sub>6</sub>, with opposite trends observed in aqueous and ethanolic media. In ethanolic media, where the material remains stable, higher Ag content leads to diminished photocatalytic activity, likely due to increased charge carrier recombination, as supported by DFT results. In contrast, in aqueous media, increasing Ag content systematically enhances photocatalytic performance, a phenomenon attributed to the instability of metal-halide perovskites in water. Their decomposition generates a BiOCl/AgCl or BiOCl/AgCl/Ag heterojunctions, which exhibit superior photocatalytic properties compared to the BiOCl formed from Ag-free samples. These findings emphasize the importance of assessing the photocatalytic behavior of metal-halide perovskites in aqueous media and highlight how their poor stability can be strategically exploited for the in situ formation of heterojunction-type photocatalysts with enhanced activity.

## ASSOCIATED CONTENT

## **Supporting Information**

The Supporting Information is available free of charge at https://pubs.acs.org/doi/10.1021/acs.jpcc.5c03037.

Additional figures, tables, and analyses including electronic structure calculations, optical characterization, photocatalytic degradation kinetics in aqueous and ethanolic media, structural refinement, charge carrier properties of BiOCl and AgCl, and reusability tests of  $Cs_2Ag_xNa_{1-x}BiCl_6$  perovskite photocatalysts (PDF)

# AUTHOR INFORMATION

## **Corresponding Authors**

Elias Paiva Ferreira-Neto — Institute of Chemistry, São Paulo State University (UNESP), Araraquara, SP 14800-060, Brazil; Email: elias.p.ferreira@unesp.br

Danilo Manzani — São Carlos Institute of Chemistry, University of São Paulo (USP), São Carlos, SP 13560-970, Brazil; ⊚ orcid.org/0000-0001-7280-5404; Email: dmanzani@usp.br

#### **Authors**

Luan do Nascimento Passini – São Carlos Institute of Chemistry, University of São Paulo (USP), São Carlos, SP 13560-970, Brazil

Bianca Oliveira Mattos — São Carlos Institute of Chemistry, University of São Paulo (USP), São Carlos, SP 13560-970, Brazil

Jéssica de Bona – Department of Chemistry, Federal University of Santa Catarina (UFSC), Florianópolis, SC 88040-380, Brazil

Luis Henrique da Silveira Lacerda — Department of Chemistry, Federal University of Santa Catarina (UFSC), Florianópolis, SC 88040-380, Brazil; orcid.org/0000-0001-5926-7074

Ubirajara Pereira Rodrigues-Filho — São Carlos Institute of Chemistry, University of São Paulo (USP), São Carlos, SP 13560-970, Brazil; orcid.org/0000-0001-6913-8540

Complete contact information is available at: https://pubs.acs.org/10.1021/acs.jpcc.5c03037

## **Funding**

The Article Processing Charge for the publication of this research was funded by the Coordenacao de Aperfeicoamento de Pessoal de Nivel Superior (CAPES), Brazil (ROR identifier: 00x0ma614).

#### **Notes**

The authors declare no competing financial interest.

## ACKNOWLEDGMENTS

This work was supported by the Brazilian Federal Agency for Support and Evaluation of Graduate Education (CAPES, Brazil, financial code 001) and the National Council for Scientific and Technological Development (CNPq, Brazil). L.H.S.L. acknowledges the National Laboratory for Scientific Computing (LNCC/MCTI, Brazil) for providing HPC resources from the SDumont supercomputer, which contributed to the research results reported in this work. This work used resources of the "Centro Nacional de Processamento de Alto Desempenho em São Paulo (CENAPAD-SP)." D.M., E.P.F.-N. and U.P.R.-F. thank CNPq for financial support (Grants 405048/2021-1, 407414/2023-1, 405282/ 2022-2, 407747/2022-2, 303117/2021-4, 304718/2023-8), U.P.R.-F. acknowledges the financial support from the National Institute of Science and Technology "Nanomaterials for Life" (INCT-Nanovida), funded by CNPq grant number 406079/2022. D.M. and U.P.R.-F. acknowledges the São Paulo Research Foundation (FAPESP) through grants 2018/19785-1, 2022/08020-0, 2022/11983-4, and 2021/08111-2. In accordance with ACS Publications policies, authors acknowledge ChatGPT 4.0 Large Language Model (OpenAI) for improving grammar and language of this manuscript.

#### REFERENCES

- (1) Liu, J.; Qi, W.; Xu, M.; Thomas, T.; Liu, S.; Yang, M. Piezocatalytic Techniques in Environmental Remediation. *Angew. Chem., Int. Ed.* **2023**, 62 (5), No. e202213927.
- (2) Dhiman, P.; Rana, G.; Kumar, A.; Sharma, G.; Vo, D.-V. N.; Naushad, M. ZnO-Based Heterostructures as Photocatalysts for Hydrogen Generation and Depollution: A Review. *Environ. Chem. Lett.* **2022**, 20 (2), 1047–1081.
- (3) Zhang, Q.; Chen, J.; Gao, X.; Che, H.; Wang, P.; Ao, Y. In-Depth Insight into the Mechanism on Photocatalytic Synergistic Removal of Antibiotics and Cr (VI): The Decisive Effect of Antibiotic Molecular Structure. *Appl. Catal., B* **2022**, *313*, No. 121443.
- (4) Allah, M. A. A. H.; Alshamsi, H. A. Facile Green Synthesis of ZnO/AC Nanocomposites Using Pontederia Crassipes Leaf Extract and Their Photocatalytic Properties Based on Visible Light Activation. *J. Mater. Sci.: Mater. Electron.* **2023**, 34 (16), No. 1263.
- (5) Saleh, T. S.; Badawi, A. K.; Salama, R. S.; Mostafa, M. M. M. Design and Development of Novel Composites Containing Nickel Ferrites Supported on Activated Carbon Derived from Agricultural Wastes and Its Application in Water Remediation. *Materials* **2023**, *16* (6), No. 2170.
- (6) Rayaroth, M. P.; Marchel, M.; Boczkaj, G. Advanced Oxidation Processes for the Removal of Mono and Polycyclic Aromatic Hydrocarbons A Review. *Sci. Total Environ.* **2023**, *857*, No. 159043. (7) Bi, T.; Du, Z.; Chen, S.; He, H.; Shen, X.; Fu, Y. Preparation of Flower-like ZnO Photocatalyst with Oxygen Vacancy to Enhance the

- Photocatalytic Degradation of Methyl Orange. Appl. Surf. Sci. 2023, 614, No. 156240.
- (8) Wang, H.; Wan, Y.; Yin, S.; Xu, M.; Zhao, X.; Liu, X.; Song, X.; Wang, H.; Zhu, C.; Huo, P. Boosting Mineralized Organic Pollutants by Using a Sulfur-Vacancy CdS Photocatalyst. *Chem. Commun.* **2023**, 59 (61), 9356–9359.
- (9) Tao, L.; Wang, J.; Luo, Z.; Ren, J.; Yin, D. Fabrication of an S-Scheme Heterojunction Photocatalyst MoS <sub>2</sub> /PANI with Greatly Enhanced Photocatalytic Performance. *Langmuir* **2023**, 39 (32), 11426–11438.
- (10) Desseigne, M.; Madigou, V.; Coulet, M.-V.; Heintz, O.; Chevallier, V.; Arab, M. Au/WO3 Nanocomposite Based Photocatalyst for Enhanced Solar Photocatalytic Activity. *J. Photochem. Photobiol., A* **2023**, 437, No. 114427.
- (11) Li, Z.; Wang, S.; Wu, J.; Zhou, W. Recent Progress in Defective TiO2 Photocatalysts for Energy and Environmental Applications. *Renewable Sustainable Energy Rev.* **2022**, *156*, No. 111980.
- (12) Mansurov, R. R.; Zverev, V. S.; Safronov, A. P. Dynamics of Diffusion-Limited Photocatalytic Degradation of Dye by Polymeric Hydrogel with Embedded TiO2 Nanoparticles. *J. Catal.* **2022**, *406*, 9–18.
- (13) Chen, Z.; Chen, H.; Wang, K.; Chen, J.; Li, M.; Wang, Y.; Tsiakaras, P.; Song, S. Enhanced TiO <sub>2</sub> Photocatalytic 2 e <sup>-</sup> Oxygen Reduction Reaction via Interfacial Microenvironment Regulation and Mechanism Analysis. *ACS Catal.* **2023**, *13* (10), 6497–6508.
- (14) Wu, Z.; Tüysüz, H.; Besenbacher, F.; Dai, Y.; Xiong, Y. Recent Developments in Lead-Free Bismuth-Based Halide Perovskite Nanomaterials for Heterogeneous Photocatalysis under Visible Light. *Nanoscale* **2023**, *15* (12), 5598–5622.
- (15) Avugadda, S. K.; Castelli, A.; Dhanabalan, B.; Fernandez, T.; Silvestri, N.; Collantes, C.; Baranov, D.; Imran, M.; Manna, L.; Pellegrino, T.; Arciniegas, M. P. Highly Emitting Perovskite Nanocrystals with 2-Year Stability in Water through an Automated Polymer Encapsulation for Bioimaging. ACS Nano 2022, 16 (9), 13657—13666.
- (16) Dudipala, K. R.; Le, T.; Nie, W.; Hoye, R. L. Z. Halide Perovskites and Their Derivatives for Efficient, High-Resolution Direct Radiation Detection: Design Strategies and Applications. *Adv. Mater.* **2024**, *36* (8), No. 2304523.
- (17) Zaccaria, F.; Zhang, B.; Goldoni, L.; Imran, M.; Zito, J.; van Beek, B.; Lauciello, S.; De Trizio, L.; Manna, L.; Infante, I. The Reactivity of CsPbBr <sub>3</sub> Nanocrystals toward Acid/Base Ligands. *ACS Nano* **2022**, *16* (1), 1444–1455.
- (18) Park, S.; Chang, W. J.; Lee, C. W.; Park, S.; Ahn, H.-Y.; Nam, K. T. Photocatalytic Hydrogen Generation from Hydriodic Acid Using Methylammonium Lead Iodide in Dynamic Equilibrium with Aqueous Solution. *Nat. Energy* **2017**, *2* (1), No. 16185.
- (19) Feng, S.; Ning, S.; Wang, L.; Zhao, J.; Ou, J.; Wu, Z.; Luo, S.; Lin, Z.; Yan, K.; Wu, C.; Xu, Y. Modifying CsPbX <sub>3</sub> (X = Cl, Br, I) with a Zeolitic Imidazolate Framework through Mechanical Milling for Aqueous Photocatalytic H <sub>2</sub> Evolution. ACS Appl. Energy Mater. **2022**, 5 (5), 6248–6255.
- (20) Cheng, J.; Mu, Y.; Wu, L.; Liu, Z.; Su, K.; Dong, G.; Zhang, M.; Lu, T. Acetate-Assistant Efficient Cation-Exchange of Halide Perovskite Nanocrystals to Boost the Photocatalytic CO2 Reduction. *Nano Res.* **2022**, *15* (3), 1845–1852.
- (21) Shang, Y.; Sun, H.; Yu, R.; Zhang, F.; Liang, X.; Li, H.; Li, J.; Yan, Z.; Zeng, T.; Chen, X.; Zeng, J. Quantitative Time-Resolved Visualization of Catalytic Degradation Reactions of Environmental Pollutants by Integrating Single-Drop Microextraction and Fluorescence Sensing. *Environ. Sci. Technol.* 2023, 57 (30), 11231–11240.
- (22) Hauptman, M.; Bruccoleri, R.; Woolf, A. D. An Update on Childhood Lead Poisoning. *Clin. Pediatr. Emerg. Med.* **2017**, 181–192, DOI: 10.1016/j.cpem.2017.07.010.
- (23) Ren, M.; Qian, X.; Chen, Y.; Wang, T.; Zhao, Y. Potential Lead Toxicity and Leakage Issues on Lead Halide Perovskite Photovoltaics. *J. Hazard. Mater.* **2022**, *426*, No. 127848.

- (24) Ye, Y.; Yin, Y.; Chen, Y.; Li, S.; Li, L.; Yamauchi, Y. Metal-Organic Framework Materials in Perovskite Solar Cells: Recent Advancements and Perspectives. *Small* **2023**, *19* (25), No. e2208119.
- (25) López-Fernández, I.; Valli, D.; Wang, C.; Samanta, S.; Okamoto, T.; Huang, Y.; Sun, K.; Liu, Y.; Chirvony, V. S.; Patra, A.; et al. Lead-Free Halide Perovskite Materials and Optoelectronic Devices: Progress and Prospective. *Adv. Funct. Mater.* **2024**, *34* (6), No. 2307896.
- (26) Wu, H.; Wang, Y.; Liu, A.; Wang, J.; Kim, B. J.; Liu, Y.; Fang, Y.; Zhang, X.; Boschloo, G.; Johansson, E. M. J. Methylammonium Bromide Assisted Crystallization for Enhanced Lead-Free Double Perovskite Photovoltaic Performance. *Adv. Funct. Mater.* **2022**, 32 (14), No. 2109402.
- (27) Guo, K.; Lin, P.; Wu, D.; Shi, Z.; Chen, X.; Han, Y.; Tian, Y.; Li, X. Cs<sub>2</sub>AgBiCl<sub>6</sub>: A Novel, High-Efficient and Stable Visible-Light Photocatalyst for Degradation of Organic Dyes. *Chem. Eur. J.* **2023**, 29 (35), No. e202300400.
- (28) Dakshinamurthy, A. C.; Sudakar, C. Bandgap Engineering and Sublattice Distortion Driven Bandgap Bowing in Cs2Ag1- x Na x BiCl6 Double Perovskites. *Appl. Phys. Lett.* **2021**, *118* (13), No. 131902, DOI: 10.1063/5.0046423.
- (29) Chini, M. K.; Srinivasan, S. G.; Tailor, N. K.; Yukta; Salahub, D.; Satapathi, S. Lead-Free, Stable Mixed Halide Double Perovskites Cs<sub>2</sub>AgBiBr<sub>6</sub> and Cs<sub>2</sub>AgBiBr<sub>6-x</sub>Cl<sub>x</sub> A Detailed Theoretical and Experimental Study. *Chem. Phys.* **2020**, *529*, No. 110547.
- (30) Rietveld, H. M. A Profile Refinement Method for Nuclear and Magnetic Structures. J. Appl. Crystallogr. 1969, 2 (2), 65-71.
- (31) Toby, B. H. EXPGUI, a Graphical User Interface for GSAS. J. Appl. Crystallogr. 2001, 34 (2), 210-213.
- (32) Filip, M. R.; Hillman, S.; Haghighirad, A. A.; Snaith, H. J.; Giustino, F. Band Gaps of the Lead-Free Halide Double Perovskites Cs2BiAgCl6 and Cs2BiAgBr6 from Theory and Experiment. *J. Phys. Chem. Lett.* **2016**, 7 (13), 2579–2585.
- (33) Hull, S.; Keen, D. A. Pressure-Induced Phase Transitions in AgCl, AgBr, and AgI. *Phys. Rev. B* **1999**, *59* (2), No. 750.
- (34) Andrade, A. O. C.; da Silveira Lacerda, L. H.; Júnior, M. M. L.; Sharma, S. K.; da Costa, M. E. H. M.; Alves, O. C.; Santos, E. C. S.; dos Santos, C. C.; de Menezes, A. S.; San-Miguel, M. A.; et al. Enhanced Photocatalytic Activity of BiOBr/ZnWO<sub>4</sub> Heterojunction: A Combined Experimental and DFT-Based Theoretical Approach. *Opt. Mater.* 2023, 138, No. 113701.
- (35) Freysoldt, C.; Grabowski, B.; Hickel, T.; Neugebauer, J.; Kresse, G.; Janotti, A.; Van de Walle, C. G. First-Principles Calculations for Point Defects in Solids. *Rev. Mod. Phys.* **2014**, *86* (1), 253–305.
- (36) Oba, F.; Kumagai, Y. Design and Exploration of Semiconductors from First Principles: A Review of Recent Advances. *Appl. Phys. Express* **2018**, *11* (6), No. 060101.
- (37) Yu, J.; Zhou, P.; Li, Q. New Insight into the Enhanced Visible-Light Photocatalytic Activities of B-, C- and B/C-Doped Anatase TiO2 by First-Principles. *Phys. Chem. Chem. Phys.* **2013**, *15* (29), 12040–12047.
- (38) Ma, X.; Dai, Y.; Guo, M.; Huang, B. The Role of Effective Mass of Carrier in the Photocatalytic Behavior of Silver Halide-Based Ag@ AgX (X = Cl, Br, I): A Theoretical Study. *ChemPhysChem* **2012**, *13* (9), 2304–2309.
- (39) Erba, A.; Desmarais, J. K.; Casassa, S.; Civalleri, B.; Donà, L.; Bush, I. J.; Searle, B.; Maschio, L.; Edith-Daga, L.; Cossard, A.; et al. CRYSTAL23: A Program for Computational Solid State Physics and Chemistry. J. Chem. Theory Comput. 2023, 19 (20), 6891–6932.
- (40) Tran, F.; Laskowski, R.; Blaha, P.; Schwarz, K. Performance on Molecules, Surfaces, and Solids of the Wu-Cohen GGA Exchange-Correlation Energy Functional. *Phys. Rev. B* **2007**, *75* (11), No. 115131.
- (41) Demichelis, R.; Civalleri, B.; Ferrabone, M.; Dovesi, R. On the Performance of Eleven DFT Functionals in the Description of the Vibrational Properties of Aluminosilicates. *Int. J. Quantum Chem.* **2010**, *110* (2), 406–415.

- (42) Gray, M. B.; Majher, J. D.; Strom, T. A.; Woodward, P. M. Broadband White Emission in Cs2AgIn1- XBixCl6 Phosphors. *Inorg. Chem.* **2019**, *58*, 13403–13410.
- (43) Morrs, L. R.; Robinson, W. R. Crystal Structure of Cs 2 NaBiCl 6. Acta Crystallogr., Sect. B 1972, 28, 653–654.
- (44) Jiang, J.; Niu, G.; Sui, L.; Wang, X.; Zhang, Y.; Che, L.; Wu, G.; Yuan, K.; Yang, X. Transformation between the Dark and Bright Self-Trapped Excitons in Lead-Free Double-Perovskite Cs 2 NaBiCl 6 under Pressure. J. Phys. Chem. Lett. 2021, 12, 7285–7292.
- (45) Zhang, L.; Fang, Y.; Sui, L.; Yan, J.; Wang, K.; Yuan, K.; Mao, W. L.; Zou, B. Tuning Emission and Electron-Phonon Coupling in Lead-Free Halide Double Perovskite Cs2AgBiCl6 under Pressure. ACS Energy Lett. 2019, 4, 2975–2982.
- (46) Ossikovski, R.; Picardi, G.; Ndong, G.; Chaigneau, M. Raman Spectroscopy and Polarization: Selected Case Studies. *C. R. Phys.* **2012**. *13* (8), 837–852.
- (47) Koniakhin, S. V.; Utesov, O. I.; Yashenkin, A. G. Raman Peak Shift and Broadening in Crystalline Nanoparticles with Lattice Impurities. *Diamond Relat. Mater.* **2024**, *146*, No. 111182.
- (48) Makuła, P.; Pacia, M.; Macyk, W. How To Correctly Determine the Band Gap Energy of Modified Semiconductor Photocatalysts Based on UV-Vis Spectra. *J. Phys. Chem. Lett.* **2018**, *9*, 6814–6817.
- (49) Filip, M. R.; Hillman, S.; Haghighirad, A. A.; Snaith, H. J.; Giustino, F. Band Gaps of the Lead-Free Halide Double Perovskites Cs2BiAgCl6 and Cs2BiAgBr6 from Theory and Experiment. *J. Phys. Chem. Lett.* **2016**, *7*, 2579–2585.
- (50) Lacerda, L. H. S.; de Lazaro, S. R. Surface and Morphology Investigation of FeCrO3Material in Ilmenite-, Corundum- and Lithium Niobate- Polymorphs. *Surf. Interfaces* **2021**, 22, No. 100837.
- (51) Lacerda, L. H. S.; de Lazaro, S. R. Density Functional Theory Investigation of Rhombohedral Multiferroic Oxides for Photocatalytic Water Splitting and Organic Photodegradation. *J. Photochem. Photobiol.*, A 2020, 400, No. 112656.
- (52) Zhang, Z.; Liang, Y.; Huang, H.; Liu, X.; Li, Q.; Chen, L.; Xu, D. Stable and Highly Efficient Photocatalysis with Lead-Free Double-Perovskite of Cs2AgBiBr6. *Angew. Chem., Int. Ed.* **2019**, 58 (22), 7263–7267.
- (53) Toby, B. H. R Factors in Rietveld Analysis: How Good Is Good Enough? *Powder Diffr.* **2006**, 21 (1), 67–70.
- (54) Daupor, H.; Wongnawa, S. Urchinlike Ag/AgCl Photocatalyst: Synthesis, Characterization, and Activity. *Appl. Catal., A* **2014**, *473*, 59–69.
- (55) Xu, Z.; Zhang, C.; Zhang, Y.; Gu, Y.; An, Y. BiOCl-Based Photocatalysts: Synthesis Methods, Structure, Property, Application, and Perspective. *Inorg. Chem. Commun.* **2022**, *138*, No. 109277.
- (56) Adenuga, D. O.; Tichapondwa, S. M.; Chirwa, E. M. N. Facile Synthesis of a Ag/AgCl/BiOCl Composite Photocatalyst for Visible Light Driven Pollutant Removal. *J. Photochem. Photobiol., A* **2020**, 401, No. 112747.
- (57) Gao, M.; Zhang, D.; Li, H.; Pu, X.; Shao, X.; Li, W. Enhanced Photocatalytic Activity of AgCl/BiOCl Heterostructures Synthesized by a One-Pot Combustion Method. *Mater. Lett.* **2015**, *159*, 406–409.
- (58) Mousavi, M.; Habibi-Yangjeh, A.; Abitorabi, M. Fabrication of Novel Magnetically Separable Nanocomposites Using Graphitic Carbon Nitride, Silver Phosphate and Silver Chloride and Their Applications in Photocatalytic Removal of Different Pollutants Using Visible-Light Irradiation. J. Colloid Interface Sci. 2016, 480, 218–231.
- (59) Liu, J. J.; Fu, X. L.; Chen, S. F.; Zhu, Y. F. Electronic Structure and Optical Properties of Ag3PO4 Photocatalyst Calculated by Hybrid Density Functional Method. *Appl. Phys. Lett.* **2011**, 99 (19), No. 191903.
- (60) Li, Y.; Zhang, W.; Niu, J.; Chen, Y. Mechanism of Photogenerated Reactive Oxygen Species and Correlation with the Antibacterial Properties of Engineered Metal-Oxide Nanoparticles. *ACS Nano* **2012**, *6* (6), 5164–5173.
- (61) Dong, C.; Fang, W.; Yi, Q.; Zhang, J. A Comprehensive Review on Reactive Oxygen Species (ROS) in Advanced Oxidation Processes (AOPs). *Chemosphere* **2022**, *308*, No. 136205.

- (62) Bi, Z.; Wang, W.; Zhao, L.; Wang, X.; Xing, D.; Zhou, Y.; Lee, D.-J.; Ren, N.; Chen, C. The Generation and Transformation Mechanisms of Reactive Oxygen Species in the Environment and Their Implications for Pollution Control Processes: A Review. *Environ. Res.* **2024**, *260*, No. 119592.
- (63) Huang, Y.-R.; Kong, Y.; Li, H.-Z.; Wei, X.-M. Removal of Crystal Violet by Ultraviolet/Persulfate: Effects, Kinetics and Degradation Pathways. *Environ. Technol. Innovation* **2020**, *18*, No. 100780.
- (64) Wang, L.; Zhou, C.; Yuan, Y.; Jin, Y.; Liu, Y.; Jiang, Z.; Li, X.; Dai, J.; Zhang, Y.; Siyal, A. A.; et al. Catalytic Degradation of Crystal Violet and Methyl Orange in Heterogeneous Fenton-like Processes. *Chemosphere* **2023**, 344, No. 140406.
- (65) Serge-Correales, Y. E.; Ullah, S.; Ferreira-Neto, E. P.; Rojas-Mantilla, H. D.; Hazra, C.; Ribeiro, S. J. L. A UV-Visible-NIR Active Smart Photocatalytic System Based on NaYbF4:Tm3+ Upconverting Particles and Ag3PO4/H2O2 for Photocatalytic Processes under Light on/Light off Conditions. *Mater. Adv.* 2022, 3 (6), 2706–2715. (66) Yu, C.; Chen, X.; Li, N.; Zhang, Y.; Li, S.; Chen, J.; Yao, L.; Lin, K.; Lai, Y.; Deng, X. Ag3PO4-Based Photocatalysts and Their Application in Organic-Polluted Wastewater Treatment. *Environ. Sci. Pollut. Res.* 2022, 29 (13), 18423–18439.

